RSC Advances

This article can be cited before page numbers have been issued, to do this please use: A. Sharma, M. Varshney, J. Park, T. K. Ha, K. H. Chae and H. Shin, *RSC Adv.*, 2015, DOI: 10.1039/C4RA16217J.

ROYAL SOCIETY OF CHEMISTRY

www.rsc.org/advances

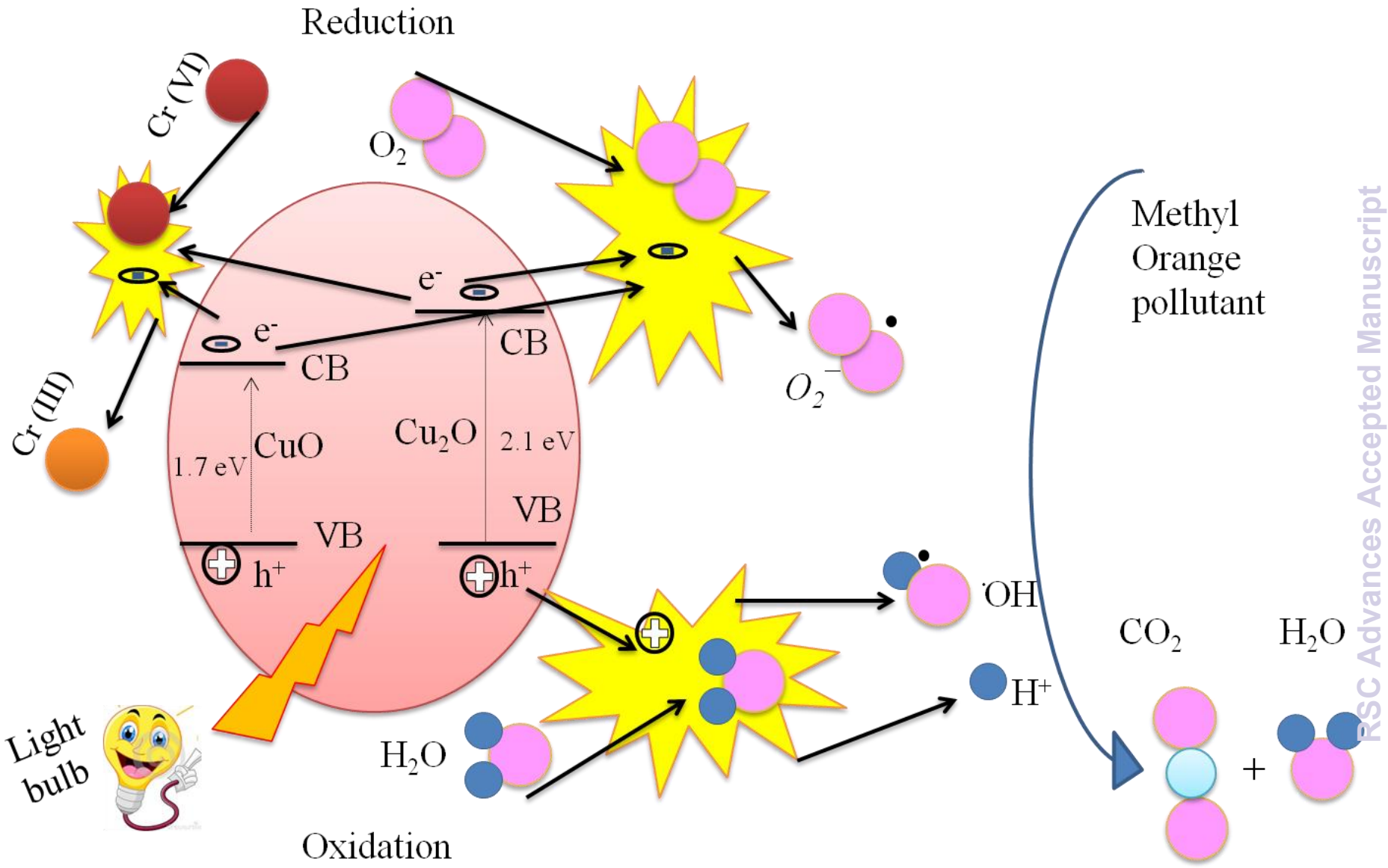

View Article Online
DOI: 10.1039/C4RA16217J

XANES, EXAFS and Photocatalytic investigations on copper oxide Nanoparticles and Nanocomposites

Aditya Sharma[1*], Mayora Varshney[1], Jae-Hun Park[1], Tae-Kyun Ha[1], Keun-Hwa Chae[2] and Hyun-Joon Shin[1ψ]

1. Pohang Accelerator Laboratory, POSTECH, Pohang 790-784, South Korea
2. Advanced Analysis Center, Korea Institute of Science and Technology, Seoul 136-791, South Korea

Abstract

CuO nanoparticles (NPs), Cu_2O/CuO and CuO/TiO_2 nanocomposites (NCs) have been synthesized by using modified co-precipitation method with three different schemes of synthesis. Crystal structure and morphology of the samples have been investigated by the synchrotron X-ray diffraction and transmission electron microscopy, respectively. The detailed local electronic structure of NPs and NCs has been determined by the X-ray absorption near edge structure (XANES) and the extended X-ray absorption fine structure (EXAFS) spectroscopy. O K-edge, Cu K- and Cu L-edge XANES spectra revealed the dominating +2 valence state of Cu in case of CuO NPs and CuO/TiO_2 NCs, although Cu^{+1} was dominated in the Cu_2O/CuO NCs. A comparison of local atomic structure around the Cu sites revealed the shorter Cu – O bond distances in the as-synthesized samples with respect to the bulk CuO or Cu_2O. The Ti K-edge EXAFS fittings for CuO/TiO_2 NCs revealed that the local anatase TiO_2 phase has been formed, with Ti – O bond distance of 1.98 Å. We further demonstrated that the CuO NPs, Cu_2O/CuO and CuO/TiO_2 NCs can serve as effective photocatalyst towards the degradation of two novel water

View Article Online
DOI: 10.1039/C4RA16217J

pollutants, (i) methyl orange (MO) and (ii) potassium dichromate (PD), under the visible light irradiation. It was found that the Cu_2O/CuO NCs exhibit higher photocatalytic activity towards the degradation of MO and PD than the CuO NPs or CuO/TiO_2 NCs. The mechanism of the photodegradation of MO and PD is also discussed in terms of possible chemical reactions, along with the electronic structure and surface properties of the samples.

Corresponding authors; ᵠshj001@postech.ac.kr , *adityaiuac@gmail.com

View Article Online
DOI: 10.1039/C4RA16217J

1. Introduction

Recently, nanostructures of TiO_2, SnO_2 and ZnO have been reported for their photocatalytic property towards the degradation of water pollutants by generating electron-hole pairs under the light irradiation [1-2]. These metal oxides are known as *n*-type transparent conducting oxides (TCOs) and have been utilized in the gas sensing [3], electrodes for the Li ion batteries [4], dye-sensitized solar cells [5] and medicine applications [6]. Most of these TCOs have large energy band gap (> 3 eV), which lies in the ultra violet (UV) range of the solar spectrum. Therefore, it is hard to generate electron-hole pairs, from these materials, under the visible light irradiation. This limits the photocatalytic efficiency of such TCOs in the solar light. Hence, there is thirst to develop new photocatalyst materials with low energy band gap and high photocatalytic efficiency under the visible light irradiation.

Copper oxides (CuO and Cu_2O) are known as important *p*-type semiconductor materials having direct energy band gap and unique optical and magnetic properties [7-9]. In the CuO, the lattice has a monoclinic symmetry (*m*-CuO; space group-C2/c) and each atom of this compound has four nearest neighbors of their kind. Cu atoms are at the centre of O rectangle and the O atoms are at the centre of the distorted tetrahedron of Cu [10]. The crystallographic structure of Cu_2O is highly symmetric (space group- $Pn\bar{3}m$) with six atoms per unit cell. The O atoms form a body-centered cubic lattice, and the Cu atoms are situated on the vertices of a tetrahedron around the each O atom [10]. CuO has an open Cu *3d* configuration ($3d^9$) and known to an antiferromagnetic semiconductor with energy band gap of ~ 1.7 eV. However, Cu_2O has essentially full Cu *3d* shell ($3d^{10}$) and present larger energy band gap ~ 2.1 eV [11].

View Article Online
DOI: 10.1039/C4RA16217J

By considering the low band gap energy and easy accessibility of copper oxides, there are efforts to degrade the water pollutants (methyl orange (MO), potassium dichromate (PD) and phenoxazin-3-one etc.) by using the copper oxide as sensitizer in a composite photocatalyst such as, CuO/ZnO [12], CuO/zeolite [13], CuO/$BiVO_4$ [14] and CuO/Cu core-shell [15]. In these studies, the photocatalytic activity was not satisfactory when CuO or Cu_2O NPs alone were used as the photocatalyst. Few recent reports are available on the photocatalytic properties of CuO nanostructures with unusual morphology, under the UV light irradiation [16-20]. The preparation of unusual morphology requires sophisticated synthesis procedure and high operational temperature/pressure. Besides this, Cu metallic phases also formed in such synthesis methods which affect the photocatalyst performance of the products [17]. Therefore, it is desirable to develop stable catalyst materials with low cost synthesis and high efficiency. It is expected that the catalytic properties of copper oxide may, further, be tailored by maneuvering its electronic structure (either by adding of foreign elements or by making mixed polymorphs).

To understand the role of copper oxide in the catalytic reactions, it is advantageous to establish a relation between the electronic structure and catalytic activity of compounds. In most of the previous reports, X-ray photoelectron spectroscopy (XPS) has been employed to determine the oxidation state of copper [18-22]. Although, this technique often provides information regarding the oxidation state of copper in the certain thin samples but; (i) it is mainly surface probing technique and (ii) generally involves cumbersome fittings procedures because the Cu 2p XPS peaks of Cu^{+}, Cu^{+2} and metallic Cu all appears within a very narrow energy range. Therefore, other element specific techniques like X-ray absorption spectroscopy (XAS), within low and high energy range, may be favorable to investigate the local atomic structure, coordination number, valence state and hybridization of the probed atoms. In this study, we employed

View Article Online
DOI: 10.1039/C4RA16217J

modified co-precipitation synthesis for the preparation of stable CuO NPs, Cu_2O/CuO and CuO/TiO_2 NCs. Comprehensive electronic structure study by XAS and photocatalytic investigations suggest that the as prepared materials can serve as an effective photocatalyst for the degradation of MO and PD under the visible light irradiation.

2. Experimental

2.1 Synthesis of CuO NPs, CuO/Cu_2O and CuO/TiO_2 NCs

For the synthesis of copper oxide photocatalyst materials, we applied previously established co-precipitation method [23-24] with modified strategy. There were three major synthesis schemes used in the present work: (a) In the first scheme, 5 g of $Cu(CH3COO)_3.5H_2O$ (Aldrich, 99.9 purity) was mixed into 200 ml of double distilled (DI) water with constant stirring for 45 minutes at room temperature. (b) In the second scheme, 1.5 g of PVA was dissolved into 25 ml DI water and then added, with stirring, into similar set of previously prepared $Cu(CH3COO)_3.5H_2O$ solution. (c) In the third scheme, the clear solutions of $Cu(CH3COO)_3.5H_2O$ and $TiCl_4.5H_2O$ were prepared according to their molar ratio (10 mol% of Ti was taken with respect to Cu) and then mixed together with stirring. In the each scheme of synthesis, when the chemicals had been fairly dissolved, the diluted NH_4OH solution was drop-wise added under the constant stirring up to the pH ~ 9. The brown-blue colored precipitates, so formed, were washed several times with DI water and then dried at 100 °C in air. The dark brown/blue colored samples were fairly crushed in the mortar-pestle and the fine powdered samples were collected carefully. The samples, synthesized by the all there different schemes, are named as; S1 (CuO NPs), S2 (Cu_2O/CuO NCs) and S3 (CuO/TiO_2 NCs), respectively. Synthesis schemes, used chemicals, sample names and composition of samples are briefed in the Table 1.

View Article Online
DOI: 10.1039/C4RA16217J

2.2 Photocatalytic experiments

The evaluation of the photocatalytic activities of the as-synthesized samples, by monitoring the degradation of MO and PD aqueous solutions, were performed at room temperature. The procedure was as follow: (i) 0.2 g/L aqueous solutions of MO and PD were prepared in the dark and stirred for 45 minutes. (ii) 0.1 g of the as-synthesized samples were dispersed into 50 ml of previously prepared MO and PD aqueous solution and stirred for 30 minutes in dark to ensure the adsorption of MO and PD onto the catalyst surface. (iii) A commercial 150 W tungsten-filament bulb was used as a light irradiation source. To avoid the thermal effects; the bulb was kept ~ 20 inches above from the beaker, the beaker was placed in the cold water plate and the water was changed after each 15 minutes. (iv) At regular intervals (30 min), 10 ml of the suspensions were sampled and the NPs and NCs were separated by centrifugation for 10 min. (v) Changes of MO and PD concentrations with irradiation time were monitored by measuring the UV-visible absorption spectra.

2.3 Characterization

The crystal structure and phases of as-prepared samples were characterized using the synchrotron X-ray diffraction (λ = 1.240 Å) performed at X-ray scattering beam line (3D beam line of Pohang Accelerator laboratory (PAL), South Korea). The morphology and crystallite sizes were studied with JOEL-JEM-2200FS high resolution transmission electron microscope (HR-TEM) accompanied with selected area electron diffraction (SAED). To prepare the samples for the HR-TEM measurements, the powder samples were fairly dispersed in the ethanol solution using the sonicator and then suspended powders were drop-wise loaded on the carbon coated Cu grids. X-ray absorption near edge structure (XANES) spectra at the O K-edge, Cu L-edge and Ti L-edge were collected in the total electron yield (TEY) mode at 10D (PAL-KIST) beam line. The photon

View Article Online
DOI: 10.1039/C4RA16217J

energy resolution of this beam line was better than 0.6 eV (at O K-edge). The extended X-ray absorption fine structure (EXAFS) measurements at Cu Kedge and Ti K-edge were performed at 1D (PAL-KIST) beam line. This beam line utilizes a Si (311) double crystal monochromator and the higher harmonics were effectively removed by detuning the crystals to 70% of the maximum intensity. Ionization chambers, filled with Ar gas, were used to record the intensity of the incident and the transmitted X-rays (the sample is placed between the first and second ionization chamber). The UV-visible absorption spectra of catalyst samples were collected by using Varian Cary-100 UV-visible spectrophotometer.

3. Results

3.1 XRD results

Fig. 1 illustrates the XRD patterns of as-synthesized samples. All of the XRD spectra were analyzed by *Powder X* software. The diffraction patterns of sample S1 fairly resemble to the monoclinic phase of CuO (space group-C2/c, lattice parameters; *a =4.689 Å, b =3.426 Å, c =5.132 Å, α= γ=90°, β=99.653°).* The high intensity peak at *2θ =29.2°* and other low intense peak at *2θ=33.7°* in the sample S2 fairly resemble to the cubic Cu_2O (space group- $Pn\ \bar{3}m$, lattice parameters; *a=b=c=4.2696 Å, α=β=γ=90°).* However, some other low intensity diffraction peaks at 28.3°, 39.8° and 48.6° match with the monoclinic CuO. Thus the sample S2 reveals the formation of composite Cu_2O/CuO phases. The diffraction peaks of sample S3 fairly match with the CuO phase, while the peaks at 25.5° and 31.6° were roughly fitted with either Ti_2O_3 rhombohedral phase or TiO_2 anatase phase. Since the rhombohedral Ti_2O_3 is known to an unstable phase of titanium oxide, the XRD patterns of sample S3 suggest the formation of copper oxide and titanium oxide composite phases. The average grain size was calculated using the Scherrer relation; $D = 0.9\lambda/\beta\cos\theta$ (D is the grain size, λ is the wavelength of used X-rays and β

View Article Online
DOI: 10.1039/C4RA16217J

is the full width at half maximum of the diffraction peak). The estimated grain sizes of all three samples are tabulated in the Table 1.

3.2 TEM-SAED results

Fig. 2 (a), (b) and (c) show the TEM images of samples S1, S2 and S3 respectively. Left and right insets in each image show the size distribution histograms and SAED patterns, respectively. The size distribution of nanoparticles is tabulated in the Table 1. The encircled area in the TEM images shows the closer view of the particles and crystallographic planes. The ring patterns in the SAED images are convincing the crystalline nature of the samples. However, aggregation of NPs is visible in all of the TEM images. Such aggregation is expected in the wet chemically synthesized samples due to the, marginal, presence of hydroxyl groups with the NPs surface [23-24].

3.3 O K edge XANES

XANES measurements probe the density of states of empty/partially filled electronic states by considering the excitation of an inner shell electron to those states that are allowed by dipole selection rule [25-26]. The major feature in the O K-edge spectra of various transition metal oxide compounds can be rationalized using the molecular orbital theory [26]. According to this, O K-edge XANES features are the result of a transition of O *1s* electron to the various partially occupied and unoccupied molecular orbitals of the oxide, taking into account the crystal-field splitting effects. In the case of cubic or monoclinic type compounds (i.e., CeO_2, ZrO2, CuO and Cu_2O, etc.) the metal d_{xy}, d_{xz} and d_{yz} orbitals point towards the oxygen atoms, while the $d_{x^2-y^2}$ and d_{z^2} orbitals point between the ligands. As a result, the e_g (group of $d_{x^2-y^2}$ and d_{z^2}) orbital lowered in energy and the t_{2g} orbital (group of the d_{xy}, d_{xz}, and d_{yz}) rose in energy [26]. The energy

View Article Online
DOI: 10.1039/C4RA16217J

difference between e_g and t_{2g} is called crystal-field splitting parameter and represented by *10 Dq*. Fig.3 presents the feature rich O K-edge XANES spectra of as-synthesized samples. There are four major peaks present in the O K-edge spectra of sample S1 at 531.8 eV, 536.5 eV, 540.6 eV and 545.3 eV, respectively. The first peak in the spectrum of sample S1 can be assigned to a $1s \rightarrow 3e_g$ transition of CuO [27]. The $3e_g$ orbital is partially filled because of d^9 configuration of Cu^{+2} in CuO and is formed by the hybridization of O 2p and Cu 3d states [27]. Rest of the peaks at higher energy are due to the transitions to the hybridize orbitals of O (*2p* and *3p*) and Cu (*4s* and *4p*) [27]. The energy separation of the first two peaks (*~4.6 eV)* is consistent with the previous reports [25, 27] and strengthened the formation of dominating CuO phase in the first synthesis scheme. Interesting variations has been observed in the spectrum of sample S2 with the presence of peak like feature ~ 534.4 eV (marked by asterisk). The previous reports have shown that Cu_2O exhibited $1s \rightarrow e_g$ transition at higher energy (~2.7 eV) than that of CuO [27]. In the present study, too, this peak is ~ 2.6 eV higher in the energy over the $1s \rightarrow 3e_g$ transition peak (at 531.8 eV) of CuO polymorphs, suggesting the formation of, mixed, Cu_2O and CuO phases in the sample S2. The intensity of first peak (at 531.8 eV) is quite lower in the sample S2, indicating low concentration of CuO phase in this sample. The sample S3, also, exhibits remarkable changes in the O K-edge features (marked by down arrows). Except the four sharp features of CuO phase, there are two more features present at 533.2 eV and 537.9 eV. These spectral features did not match with the spectral features of CuO and Cu_2O phases and may arise due to the hybridization of O *2p* orbitals with titanium *d* obitals. Appearance of such features is intriguing and requires detailed investigations. In this regard, we have collected Ti L-edge and Ti K-edge XANES and Ti K-edge EXAFS spectra from this sample and shall be discussed in the following sections of the paper.

View Article Online
DOI: 10.1039/C4RA16217J

3.4 Cu K-edge XANES

To further investigate the structural and electronic structure differences in the as synthesized samples, Cu K-edge XANES spectra were collected and have been presented in the Fig. 4. It is clear from the Fig.4 that the sample S1 shows intense white line peak at 8995.6 eV, shakedown like feature at 8986.1 eV and weak absorption pre-edge feature at 8972 eV which are attributed to the *1s→4p* (continuum), *1s→4p$_z$* features of CuO (Cu in +2 valence state) and *1s→3d* transition, respectively [28-29]. The *1s→3d* is forbidden transition by the dipole selection rules, and, thus, the *1s→3d* pre-edge feature is attributed to the *3d+4p* orbital mixing as well as vibronic coupling and direct quadrupole coupling [29]. In the previous reports, this dipole-forbidden transition is considered as the identification of +2 valence state of Cu, because this pre-edge feature is not observed in the compounds of Cu^{+1}[30]. In the Cu^{+1} compounds, the *1s→3d* transition does not exist because of the d^{10} closed shell configuration. The closer examination of pre-edge feature (see the inset of Fig. 4) revealed that this feature is present in the S1 and S3 samples and absent in case of S2 sample, indicating dominating +2 valence state of Cu in the samples S1 and S3. Interesting variations in the spectral features and peak position have been observed in the XANES spectrum of sample S2. The white line position shifts to the lower photon energy (8993.2 eV) and an apparent shoulder ~ 8979.3 eV is also present in the spectrum. The Cu K-edge position has been reported to shifts towards the lower energy as the oxidation state of Cu decreases and the Cu_2O presents remarkable shoulder at ~9 eV beneath the white line peak [28]. Here, the intense white line peak and the dominant shoulder, in the sample S2, can be assigned to the *1s→4p* (continuum) and *1s→4p$_{x,y}$ p$_z$* transition of Cu_2O (Cu in +1 valence state), respectively [28]. Therefore, the Cu K-edge structural features of sample S2 validate the formation of dominating Cu_2O phase in the second scheme of synthesis, as

View Article Online
DOI: 10.1039/C4RA16217J

evidenced by XRD results. The pre-edge, shakedown feature and white line peak positions of S3 sample fairly match with the spectral features of sample S1. Furthermore, we could not observe significant variations in the Cu K-edge spectral features of this sample due to the presence of titanium oxide phases, as they were observed in the XRD spectra. This signifies the dominating local CuO structure and minor titanium oxide phases in the sample S3. To further probe the valence state of Cu in the as-synthesized samples, systematic, Cu $L_{3,2}$-edge XANES measurements were performed and shall be discussed in the following section.

3.5 Cu L-edge, Ti L-edge, and Ti K-edge XANES

Since the Cu L-edge XANES spectrum represents the dipole transitions of Cu $2p_{3/2}$ and $2p_{1/2}$ electrons into the empty *d*-states [27, 31-32], therefore, in order to probe the *3d* character of Cu in as-synthesized samples the Cu $L_{3,2}$-edge XANES spectra were collected from all three samples and presented in the Fig. 5. It is clear from the Fig. 5 that sample S1 shows two distinct peaks at 935.4 eV and 955.3 eV. These two features are assigned to the transitions from Cu $2p_{3/2}$ (L_3) and $2p_{1/2}$ (L_2) electrons into the empty *d*-states, respectively [27, 31-32]. Presence of a bump like feature at ~943.1 eV and the energy separation between L_3 and L_2 edge (19.9 eV) are consistent with the reported values [27] and, thus, signify the formation of CuO phase (Cu is +2 valence state) in this sample. Noticeable changes in the spectral features can be seen in the sample S2. There are three major differences in the L edge spectra between sample S1 and S2: (i) the peak position of Cu L-edge features of sample S2 appears at higher energy than those of sample S1, (ii) the energy separation between L_3 and L_2 features, which is determined by the spin-orbit coupling and known to be dependent on the oxidation state of Cu [27], is lesser in the case of sample S1 and (iii) post edge peak ~938.8 eV appears in sample S2 (marked by asterisk). The spectral features and energy separation between L_3 and L_2 edges of sample S2 are quite

View Article Online
DOI: 10.1039/C4RA16217J

similar to those of reported Cu_2O thin films [27] and thus suggest the formation of Cu_2O phases (Cu is +1 valence state) in this sample. The spectral features and energy separation between L_3 and L_2 edges of sample S3 resemble to those of sample S1, indicating that valence state of Cu remains +2 in this sample. Our XRD results have shown titanium oxide phases in the sample S3 and O K-edge spectra show some intriguing features. Therefore, in order to study the valence state of Ti and local electronic structure surrounding the Ti atom, in the sample S3, the Ti L-edge and Ti K-edge XANES spectra were also collected and presented in the Fig. 6. Fig 6 (a) shows the Ti L-edge XANES spectrum of sample S3 along with the spectra of rutile phase TiO_2 (*R*-TiO_2) and anatase phase TiO_2 (*A*-TiO_2) reference samples. The Ti L-edge spectrum of sample S3 demonstrates four sharp features at 459.4 eV, 461.2 eV, 464.8 eV and 467.1 eV, namely *i*, *j*, *k*, and *l*, respectively. The first two features constitute L_3 edge and last two features contribute to the L_2 edge [33]. Interestingly, pre-edge peak (*i'*) and L_3 second white line splitted peak (*j')* have also been appeared in the spectrum of *R*-TiO_2 and *A*-TiO_2. However, the feature *j'* appears at low energy in case of *R*-TiO_2 and at higher energy for *A*-TiO_2 [33]. The 10 Dq value and the spectral features of sample S3 fairly resemble to that of *A*-TiO_2(Ti in +4 valence state) [33] and suggesting the formation of local *A*-TiO_2 phase in the sample S3. The peak *l* of sample S3 shows, unusual, strong intensity. This is due to the overlapping of Ti L_2 edge features with the second diffraction order of Cu L_3 edge. Fig. 6 (b) shows the Ti K-edge XANES spectrum of sample S3. The spectrum is mainly divided into two regions; (i) pre-edge region (4940 to 4970 eV) and (ii) above threshold region (4970 to 5050 eV). Within the pre-edge region there are two low intense features (*m* and *n)* and a sharp pre-edge (*o*). Above the threshold there are three multiple scattering (MS) resonance features (*p*, *q*, and *r*) of the excited photoelectrons, scattered by neighbor atoms. According to recent investigations, the peak *m* is purely quadrupolar t_{2g}; *n* is

View Article Online
DOI: 10.1039/C4RA16217J

dipolar in nature but includes also a minor e_g quadrupolar component while *o* is a pure dipolar feature [34-35]. From the MS calculations [35], features *n* and *o* may be associated with the transition to unoccupied states made up by mixing of Ti-*4p* orbitals and higher-shell Ti-*3d* orbitals. The spectral features *p*, *q*, and *r* are mainly due to MS contribution of the ejected photoelectron from higher-shell neighboring atoms [34-35]. Ti K-edge XANES spectrum, above the threshold, of *A*-TiO_2 exhibits sharp *q* peak and broad/splitting *r* peak while the *R*-TiO_2 shows splitted *q* peak and intense *r* peak [36-37]. Thus the Ti K-edge spectral features of the sample S3 convince spectral features of the *A*-TiO_2 and strengthened the formation of *A*-TiO_2 in this sample, as demonstrated by XRD and Ti L-edge XANES spectra. Further, the local atomic investigations may be advantageous to probe the different phases, coordination number and bond distances between the atoms by using EXAFS analysis. The EXAFS analysis along with the Fourier transform (FT) data shall be discussed in the following section.

3.6 Cu K-edge and Ti K -edge EXAFS

To study the coordination number of metal atoms and bond distances between metal-metal and metal-oxygen atoms, we performed the EXAFS analysis at the Cu K-edge and Ti K-edge. Normalization of the raw data and background noise correction were performed using *Athena-Artemis* program package [38]. To determine the relative bond length and local atomic structure with respect to the absorbing atom, the EXAFS data were FT to the *r-space*. To simulate the FT data (in *r-space*), systematic theoretical structure of CuO was generated using the ATOM and FEFF codes [39]. The data range taken for the transformation was 2-13.5 $Å^{-1}$ in *k-space*. Structural parameters were obtained, without the phase corrections, by fitting the data in *r-space*, within the interval of 1-4 Å. The FT of k^3-weighted $\chi(k)$, along with the fit, for the Cu K-edge EXAFS of the as-synthesized samples are shown in the Fig. 7 (a-d). The shell parameters [bond-

View Article Online
DOI: 10.1039/C4RA16217J

distance *(R)*, coordination number *(N)* and Debye-Waller factor *(σ^2)*] are presented in Table 2. The first and second shells in the FTs arise from the single scattering paths of cation-oxygen and cation-cation, respectively [28]. Third and other higher shells originate from the single and MS contributions from a variety of paths and thus larger uncertainties in the third shell fitted parameters have been reported [40]. Here, we first focus on the Cu – O and Cu – Cu shells of all three samples. It is clear from the Fourier transformed EXAFS oscillations of sample S1 that a sharp feature at 1.5 Å is appeared followed by the other intense feature at 2.4 Å. The first feature corresponds to Cu – O bonds and the second feature represents the Cu – Cu bonds of CuO [28, 41]. The Fourier transformed EXAFS oscillation features of sample S2 are quite different to those of the sample S1. There are mainly three spectral features, in the sample S2, at 1.2 Å, 1.5 Å and 2.4 Å, respectively. To simulate these spectral features, we generated the theoretical structures of CuO and Cu_2O for the same sample (S2). It is clear from the Fig. 7(b) that the spectral feature at 1.5 Å was better simulated for the theoretical CuO structure; however, the peaks ~ 1.2 Å and 2.4Å were fairly resembled with the theoretical Cu_2O structure (see Fig. 7 (c)). Previous EXAFS studies have shown that the Cu – O and Cu – Cu bond distances were lower in the Cu_2O compound because of the highly symmetric cubic structure of Cu_2O and octahedral environment of Cu in Cu_2O [41]. Therefore, the first peak in the FT oscillations of sample S2 is the signature of Cu – O bond from Cu_2O phase and the second peak represents the Cu – O bond from the CuO phase. To further probe the local atomic structure around Cu, in the sample S3, the Cu K-edge EXAFS data were simulated with the theoretical CuO structure and presented in Fig. 7 (d). It is clear from the Fig. 7 (d) that Cu – O shell is well fitted, but the Cu – Cu and other higher scattering paths are not fitted with the theoretical CuO structure, which may be due the co-existence of TiO_2 phases in this sample. Similar scarce fitted EXAFS oscillations have also

View Article Online
DOI: 10.1039/C4RA16217J

been reported in the CuO/TiO_2 nanorod systems [28]. To examine the TiO_2 phase and Ti coordination with O in the sample S3, Ti K-edge EXAFS data were collected and the theoretical *A*-TiO_2 structure was generated using the *Athena- Artemis* program package with the same parameters (*k* and *r*-ranges) as applied to simulate the Cu K-edge. It is clear from the Fig. 7 (e) that *A*-TiO_2 structure is fairly simulated for the Ti K-edge EXAFS, for the sample S3, and strengthened the formation of *A*-TiO_2 phase in this sample. The Ti – O and Ti – Ti bond distances and coordination number (without phase correction) obtained from this fitting are listed in the Table 2. It can be noticed from the Table 2 that the Debye-Waller factor is higher and Cu – O and Cu – Cu bond lengths are shorten in the case of sample S2. The Debye-Waller factor represents the structural perturbations in the materials and has been reported with higher values for the small sized NPs [40]. Therefore, a large Debye-Waller factor, in the sample S2, may indicate the structural constraints because of the coexistence of small sized CuO and Cu_2O polymorphs. Further, small sized NPs possess rather high surface free energy (or large surface area) which results in a contraction of the cell parameters of the NPs [40]. Thus, in the present case of sample S2, lower Cu – O or Cu – Cu bond lengths in comparison to the reported bulk CuO or Cu_2O may be due to the size effect.

3.7 Photocatalytic activity

As a demonstration of the application of the as-synthesized samples, MO and PD were chosen as model organic dyestuffs to evaluate the photocatalytic performance. Fig. 8 (a-d) and Fig.9 (a-d) show the photocatalytic performance of all three samples towards the degradation of MO and PD, respectively. Control experiments, without any catalyst materials, were also performed for MO and PD under the same light irradiation condition. It is clear from the Fig. 8a that UV-vis absorption spectra of MO exhibit a strong absorption peak at ~465 nm and less intense peak at

View Article Online
DOI: 10.1039/C4RA16217J

~270 nm. These two absorption peaks are the typical absorptions of azobenzene of MO dye [43]. Similarly, the two major absorption peaks in PD aqueous solution (see Fig.9 (a)) appeared at ~360 nm and ~260nm and were attributed to the absorption of Cr_2O_7 ligands [44]. Interestingly, there is no measureable change in the absorption spectra of MO and PD aqueous solutions under the light irradiation when no catalyst was added. This is in accordance with the previous reports where no degradation of MO and PD could detect under the light radiation [16-19]. Fig. 8 (b)-(d) and Fig. 9 (b)-(d) show that photodegradation of MO and PD has been established under the presence of all three photocatalyst samples.

To understand the photocatalytic response of the samples, we first enlighten the working mechanism of photocatalysis which involves several key processes [15, 18-19]. In the first step of photocatalysis process, significant adsorption of pollutant dyes (MO and PD in the present case) is expected to take place on the surface of used catalyst materials. In the second step, the excitation of electrons takes place from the valance band (VB) to the conduction band (CB) of the photocatalyst material under the light irradiation (see eq. (1)). The photoelectrons are expected to scavenge by the molecular oxygen (O_2) to create the superoxide radical anion (O_2^-) (eq. (2)) and hydrogen-peroxide (H_2O_2) (eq. (3)):

$$hv \text{ (light irradiation)} + \text{Photocatalyst sample} \rightarrow e^- + h^+ \quad (1)$$

$$O_2 + e^- \rightarrow O_2^- \quad (2)$$

$$2H^+ + O_2 + 2e^- \rightarrow H_2O_2 \quad (3)$$

Either the holes or the intermediate products, produced in reactions 1-3, or both participate to generate the hydroxyl radicals [(OH^-) and ($^{\bullet}OH$)] in the solution as follows (eq. 4-5);

View Article Online
DOI: 10.1039/C4RA16217J

$$H_2O + Photocatalyst\ sample\ (h^+) \rightarrow \dot{O}H + H^+ \quad (4)$$

$$O_2^- + H_2O_2 \rightarrow O_2 + OH^- + \dot{O}H \quad (5)$$

The $\dot{O}H$ radicals work as a powerful oxidizing agent and degrade the most of the water pollutant dyes [18-19, 45]. The reactive oxygen species and holes contribute to the oxidative pathways in the degradation of organic pollutants [45] as following;

$$Organic\ Pollutants + O_2^- \rightarrow CO_2 + H_2O \quad (6)$$

$$Organic\ Pollutant + h^+ \rightarrow CO_2 + H_2O \quad (7)$$

On the other hand the electrons, in the conduction band, may reduce the $Cr_2O_7^{2-}$ ligands via the following reaction:

$$n(Cr_2O_7^{2-}) + n(OH^-) + ne^- \rightarrow n\,Cr^{+3} + n(H_2O) \quad (8)$$

In the reaction 8, the *n* is non zero and arbitrary number. We further calculated the degradation rate of MO and PD by considering the intensity of absorbance peaks, as a function of light irradiation time by using the following relation;

$$D_t = \frac{A_0 - A_t}{A_0} \times 100\ \% \quad (9)$$

where the D_t (%) is the degradation rate of MO and PD aqueous dyes at an irradiation time of *t* minutes, A_0 is the initial absorbance and A_t is the absorbance at an irradiation time of *t* minutes. Fig. 10 (a) and (b) represents the photodegradation rates of MO and PD dyes, respectively, for all three catalyst samples as a function of light irradiation time. It is clear from the Fig. 10 that the photo degradation rates of sample S1 and sample S3 are quite comparable and the sample S2

View Article Online
DOI: 10.1039/C4RA16217J

exhibits superior photodegradation rates for the MO and PD dyes under the same light irradiation condition. The higher degradation rates of sample S2 could be understand as follows;

The smaller sized NPs posse higher surface area and offer extensive adsorption reactions of the pollutants [18, 45]. Furthermore, higher migration rates of photo-generated charge carriers, towards the surface, have also been observed in case of smaller sized NPs [46]. Our XRD and TEM results have confirmed the formation of smaller sized (4 nm – 6 nm) Cu_2O/CuO NCs in sample S2, resulting the high Debye-Waller factor and shorter Cu – O bond distances in the EXAFS analysis. Such smaller sized Cu_2O/CuO NCs may offer adequate adsorption and oxidation/reduction reactions on their surface and resulting high photocatalyst performance. The schemes of the photocatalysis for all three samples are presented in the Fig. 11 (a – c). In the Fig. 11 (b), we demonstrated that the CuO and Cu_2O both work as the electron-hole generation centers and thus effectively degrade the pollutants via oxidation and reduction processes. On the other hand the sample S3, however, encloses TiO_2 crystallites along with CuO NPs but the energy of visible light photons is not sufficient to generate the electron-hole pairs from TiO_2 NPs because of the large energy band gap (~ 3.2 eV) of TiO_2. Therefore, only CuO serves as the electron-hole production center in the sample S1 and S3 (see Fig. 11 (a) and (c)) and hence lower degradation rates of MO and PD could achieve for the samples S1 and S3.

Conclusions

We have reported a modified co-precipitation method for the synthesis of CuO NPs, Cu_2O/CuO and CuO/TiO_2 NCs. XRD and TEM results illustrate the formation of crystalline NPs of disparate sizes. We adequately applied the XANES and EXAFS techniques to probe the local electronic/atomic structure of the as-synthesized samples. Spectral features and 10 Dq values in the XANES indicate the formation of typical *m*-CuO phase in the sample S1, while the XANES

View Article Online
DOI: 10.1039/C4RA16217J

spectral features at O K-edge, Cu L-edge and Cu K-edge of sample S2 authenticate the cubic Cu_2O phases in the sample S2. The Cu K-edge EXAFS spectra of S1 sample were better fitted with the monoclinic CuO structure (with Cu – O bond distance of 1.91 Å and coordination number 3.8), however partial CuO and Cu_2O theoretical structures could be produced for the sample S2 (with short bond distance 1.84 Å and coordination number 1.72 for Cu_2O phase), indicating single phase CuO formation in the sample S1 and mixed CuO and Cu_2O phases in the sample S2. Fourier transformed spectra of Cu K-edge EXAFS and Ti K-edge EXAFS validate the formation of *m*-CuO and *A*-TiO_2 phases in sample S3 and support our XANES investigations. All of the samples exhibited excellent photocatalytic properties and significantly degraded the MO and PD dye pollutants under the visible light irradiation. It is expected that higher adsorption reactions of MO and PD take place on the surface of smaller sized NPs (sample S2) and generation of the plenty of electron-hole pairs from the CuO and Cu_2O centers enhances the photocatalysis reaction under the light irradiation. In the mechanism of photocatalyst reaction, we believe that the destruction of organic dyes under the visible light irradiation by the photocatalyst material is initiated mainly through hydroxyl radicals, and the resultant water molecules.

Acknowledgment

Aditya Sharma, Mayora Varshney and Hyun-Joon Shin would like to acknowledge the financial support by the Basic Science Research Program (No. 2008-0062606, CELA-NCRC) through the National Research Foundation of Korea (NRF) and by the Converging Research Center Program (NRF-2014M3C1A8048817) through the Ministry of Science, ICT and Future Planning, Korea.

View Article Online
DOI: 10.1039/C4RA16217J

Authors are also thankfull to Dr. Nam-Suk Lee (NINT-POSTECH) and Dr. Taeyeol Jeon (3D beam line PAL) for their help in the TEM and XRD measurements.

View Article Online
DOI: 10.1039/C4RA16217J

References

1. C. Cheng, A. Amini, C. Zhu, Z. Xu, H. Song and N. Wang, Sci. Rep., 2014, **4**, 4181-4185.
2. W. Zhao, M. Zhang, Z. Ai, Y. Yang, H. Xi, Q. Shi, X. Xu and H. Shi, J Phys. Chem. C, 2014, **118**, 23117-23125.
3. L. Mei, Y. Chen and J. Ma, Sci. Rep., 2014, **4**, 6028-6036.
4. I. X. Liu, J. Zhang, W. Si, L. Xi, S. Oswald, C. Yan, and O. G. Schmidt, *Nanoscale*, 2014, (accepted article) DOI: 10.1039/C4NR04903A.
5. J. Liang, G. Zhang, Y. Yang and J. Zhang, J. Mater. Chem. A, 2014, **2**, 19841-19847.
6. K. R. Raghupathi, R. T. Koodali and A. C. Manna, Langmuir 2011, **27**, 4020-4028.
7. X. Y. Chen, H. Cui, P. Liu, and G. W. Yang, Appl. Phys. Lett., 2007, 90, 183118-183120.
8. T. Kimura, Y. Sekio, H. Nakamura, T. Siegrist, and A. P. Ramirez, Nature mat., 2008, **7**, 291-294.
9. C. Chen, L. He, L. Lai, H. Zhang, J. Lu, L. Guo and Y. Li, J. Phys.: Condens. Matter, 2009, **21,** 145601-145608.
10. J. Ghijsen, L. H. Tjeng, J. van Elp, H. Eskes, J. Westerink and G. A. Sawatzky, Phys. Rev. B, 1988, **38**, 11322-11330.
11. P. Wang, Y. H. Ng and R. Amal, Nanoscale, 2013, **5**, 2952-2958.
12. J. Yu, S. Zhuang, X. Xu, W. Zhu, B. Feng and J. Hu*, J. Mater. Chem. A*, 2014, (accepted article) DOI: 10.1039/C4TA04526B.
13. A. N. Ejhieh and S. Hushmandrad, Appl. Catal. A: Gen., 2010, **388**, 149-159.
14. W. Wang, J.Wang, Z. Wang, X. Wei, L. Liu, Q. Ren, W. Gao, Y. Lianga and H. Shia, Dalton Trans., 2014, **43**, 6735-6743.
15. T. Kou, C. Jin, C. Zhang, J. Sun and Z. Zhang, RSC Adv., 2012, **2**, 12636-12643.

View Article Online
DOI: 10.1039/C4RA16217J

16. R. Li, X. Yan, L. Yu, Z. Zhang, Q. Tang and Y. Pan, CrystEngComm, 2013, **15**, 10049.

17. S. L. Wang, P. G. Li, H. W. zhu and W. H. Tang, Pow. Technol., 2012, **230**, 48-53.

18. Z. Zheng, B. Huang, Z. wang, M. Guo, X. Qin, X. Zhang, P. Wang and Y. Dai, J. Phys. Chem. C, 2009, **113**, 14448-14453.

19. L. Huang, F. Peng, H. Yu and H. Wang, Sol. Stat. Sci., 2009, **11**, 129-138.

20. A. S. Ethiraj and D. J. Kang, Nanoscl. Res. Lett., 2012, **7**, 70-75.

21. Y. Mao, J. He, X. Sun, W. Li, X. Lu, J. Gan, Z. Liu, L. Gong, J. Chen, P. Liu and Y. Tong, Electrochim. Acta, 2012, **62**, 1-7.

22. C. Zhu, A. Osherov and M.J. Panzer, Electrochim. Acta, 2013, **111**, 771-778.

23. A. Sharma, A.P. Singh, P. Thakur, N. B. Brookes, S. Kumar, C. G. Lee, R. J. Choudhary, K.D. Verma and R. Kumar, J. Appl. Phys., 2010, **107**, 093918-093925.

24. A. Sharma, M. Varshney, H. J. Shin, Y.J. Park, M. G. Kim, T.K. Ha, K.H. Chae and S. Gautam, Phys. Chem. Chem. Phys., 2014, **16**, 19909-19916.

25. F.M. de Groot, M. Grioni, C. Fuggle, J. Ghijsen, G. A. Sawatzky and H. Petersen, Phys. Rev. B, 1989, **40**, 5715-5723.

26. J.G. Chen, Surf. Sci. Reports, 1997, **30**, 1-152.

27. A. B. Gurevich, B. E. Bent, A. V. Teplyakov and J. G. Chen, Surf. Sci., 1999, **442**, L971-L976.

28. P. Khemthong, P. Photai and N. Grisdanurak, Int. J. Hydrogen Energy, 2013, **38**, 15992-16001.

29. J. N. Nian, S. A. Chen, C. C. Tsai, and H. Teng, J. Phys. Chem. B, 2006, **110**, 25817-25824.

30. M. Vaseem, A. Umar, Y. B. Hahn, D. H. Kim, K. S. Lee, J. S. Jang and J. S. Lee, Cataly. Commun., 2008, **10**, 11-16.

View Article Online
DOI: 10.1039/C4RA16217J

31. M. Grioni, J. B. Geodkoop, R. Schoorl, F.M. de Groot, J. C. Fuggle, F. Schafers, E.E. Koch, G. Rossi, J. M. Esteva and R. Karnatak, Phys. Rev. B, 1989, **39**, 1541-1545.

32. M. Grioni, J. F. van Acker, M. T. Czyzyk, and J. C. Fuggle, Phys. Rev. B, 1992, **45**, 3309-3318.

33. E. Stoyanov, F. langenhorst and G. S. Neumann, American Mineralogist, 2007, **92**, 577-586.

34. Z. Y. Wu, G. Ouvrard, P. Gressier and C. R. Natoli, Phys. Rev. B, 1997, **55**, 10382-10391.

35. Y. Joly, D. Cabaret, H. Renevier, and C. R. Natoli, Phys. Rev. Lett., 1999, **82**, 2398-2401.

36. M. S. P. Francisco, V. R. Mastelaro, A. O., Florentino ND d. Bazin, Top., Catalys., 2002, **18**, 105-111.

37. G. A. Waychunas, American Mineralogist , 1987, **72**, 89-101.

38. B. Ravel and M. Newville, J. Synchrotron Radiat., 2005, **12**, 537–541.

39. A. L. Ankudinov and J. J. Rehr, Phys. Rev. B, 1997, **56**, R1712–R1715.

40. J-F. Lee, M-T. Tang, W. C. Shin and R. S. Liu, Mat. Res. Bul. 2002, **37**, 555-562.

41. Y. Tanizawa, T. Shido, W. J. Chun, K. Asakura, M. Nomura and Y. Iwasawa, *J. Phys. Chem. B*, 2003, **107**, 12917-12929.

42. M. C. Hsiao, H. P. Wang and Y. W. Yang, *Environ. Sci. Technol*. 2001, **35**, 2532-2535.

43. J. Oakes and P. Gratton, J. Chem. Soc., *PerkinTrans.*, 1998, **2**, 2563-2568.

44. S. K. Li, X. Guo, Y. Wang, F. Z. Huang, Y. H. Shen, X. M. Wang and A. J. Xie, *Dalton Trans.,* 2011, **40**, 6745–6750.

45. L. Pan, X. Liu, Z. Sun and C. Q. Sun, *J. Mater. Chem. A*, 2013, **1**, 8299-8326.

46. A. Hagfeldt and M. Gratzel, Chem. Rev. 1995, **95**, 49-68.

View Article Online
DOI: 10.1039/C4RA16217J

Figure captions

Fig.1 X-ray diffraction patterns of sample S1 (CuO NPs), S2 (Cu_2O/CuO NCs) and S3 (CuO/TiO_2 NCs).

Fig. 2. TEM images of (a) sample S1 (CuO NPs), (b) sample S2 (Cu_2O/CuO NCs) and (c) sample S3 (CuO/TiO_2 NCs). (Left and right insets show the histograms of size distribution and SAED patterns, respectively).

Fig.3 O K-edge XANES spectra of samples S1 (CuO NPs), S2 (Cu_2O/CuO NCs) and S3 (CuO/TiO_2 NCs). The spectra were vertically displaced for clarity.

Fig.4 Cu K-edge XANES spectra of samples S1 (CuO NPs), S2 (Cu_2O/CuO NCs) and S3 (CuO/TiO_2). The inset shows that the pre-edge features are present in S1 and S3 samples and absent in the S2 sample.

Fig. 5. Cu $L_{3,2}$-edge XANES spectra of samples S1 (CuO NPs), S2 (Cu_2O/CuO NCs) and S3 (CuO/TiO_2).

Fig. 6. (a) Ti $L_{3,2}$-edge XANES spectra of sample S3, *R*-TiO_2 and *A*-TiO_2. (b) Ti K-edge XANES spectrum of sample S3.

Fig. 7. Magnitude of FT along with fittings of; (a) sample S1 witted with the theoretical structure of CuO, (b) sample S2 fitted with theoretical structure of CuO, (c) sample S2 fitted with the theoretical structure of Cu_2O, (d) sample S3 fitted with the theoretical structure of CuO, (e) sample S3 fitted with the theoretical structure of anatase TiO_2.

View Article Online
DOI: 10.1039/C4RA16217J

Fig. 8. UV-visible absorption spectra taken at different time of; (a) MO solution without catalyst, (b) MO solution with sample S1 (CuO NPs), (c) MO solution with sample S2 (Cu_2O/CuO NCs) and (d) MO solution with sample S3 (CuO/TiO_2 NCs).

Fig. 9. UV-visible absorption spectra taken at different time of; (a) PD solution without catalyst, (b) PD solution with sample S1 (CuO NPs), (c) PD solution with sample S2 (Cu_2O/CuO NCs) and (d) PD solution with sample S3 (CuO/TiO_2 NCs).

Fig. 10. Degradation rates (%) of MO and PD for the samples S1 (CuO NPs), S2 (Cu_2O/CuO NCs) and S3 (CuO/TiO_2 NCs) as a function of light irradiation time.

Fig. 11. Schematic schemes of the generation of electron-hole pairs and degradation of MO and PD pollutants, via oxidation and reduction reactions, of; (a) sample S1, (b) sample S2 and (c) sample S3

View Article Online
DOI: 10.1039/C4RA16217J

Table captions

Table 1: Summary of synthesis schemes of samples, sample manes, particle sizes calculated by XRD and TEM and details of compounds.

Table 2. Structural parameters (obtained from the fittings of Cu K-edge and Ti K-edge EXAFS data) of first two coordination shells around the Cu and Ti atoms.

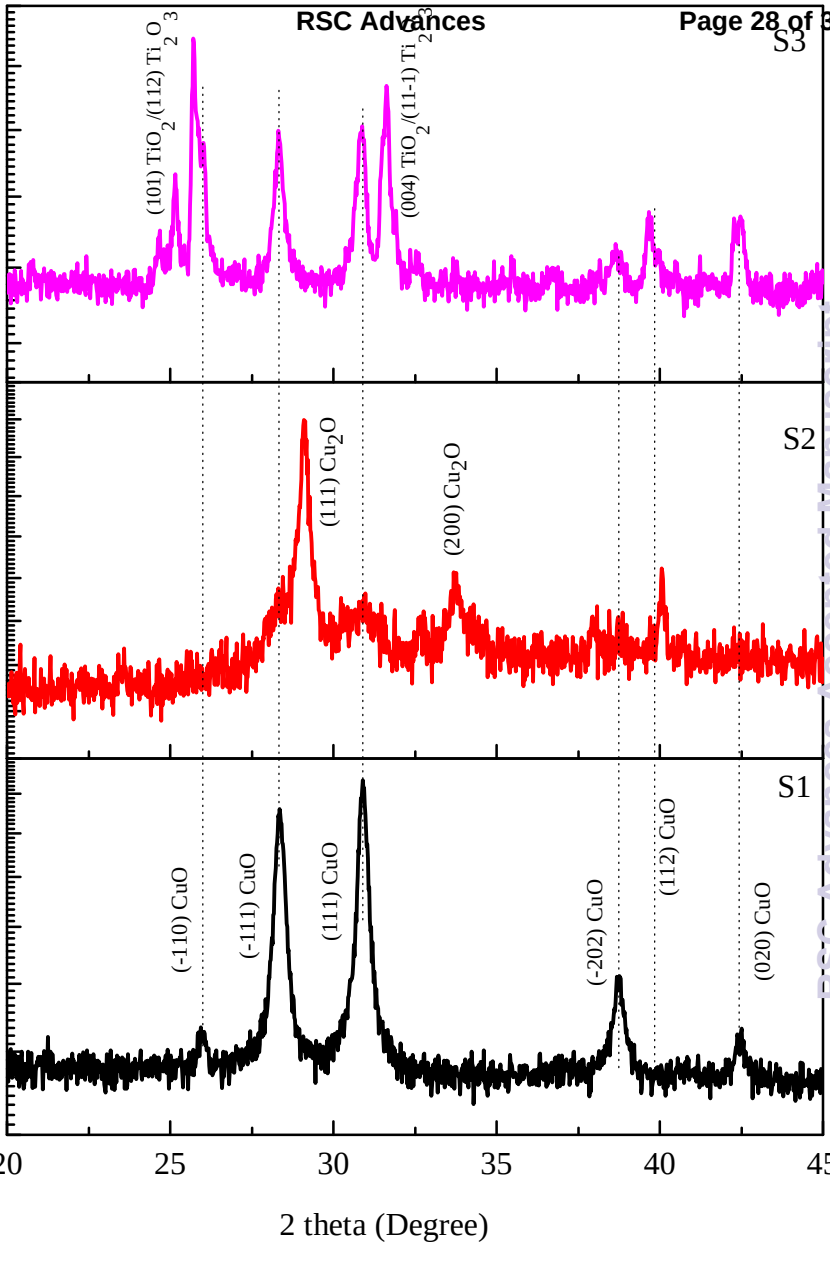

View Article Online
DOI: 10.1039/C4RA16217J

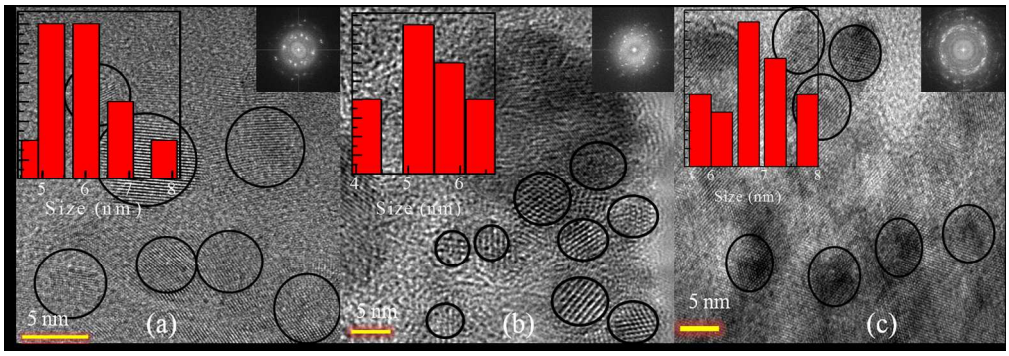

303x104mm (150 x 150 DPI)

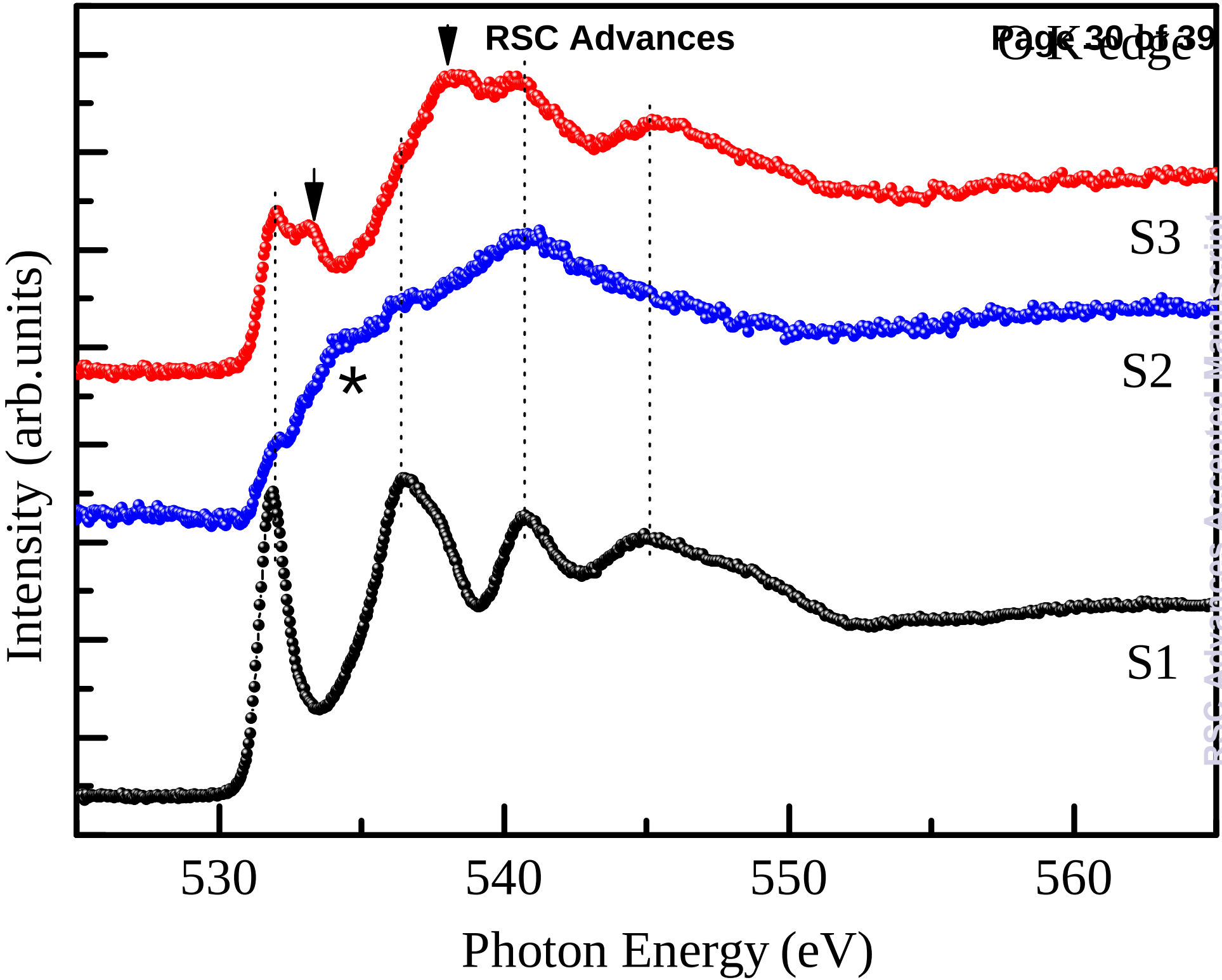

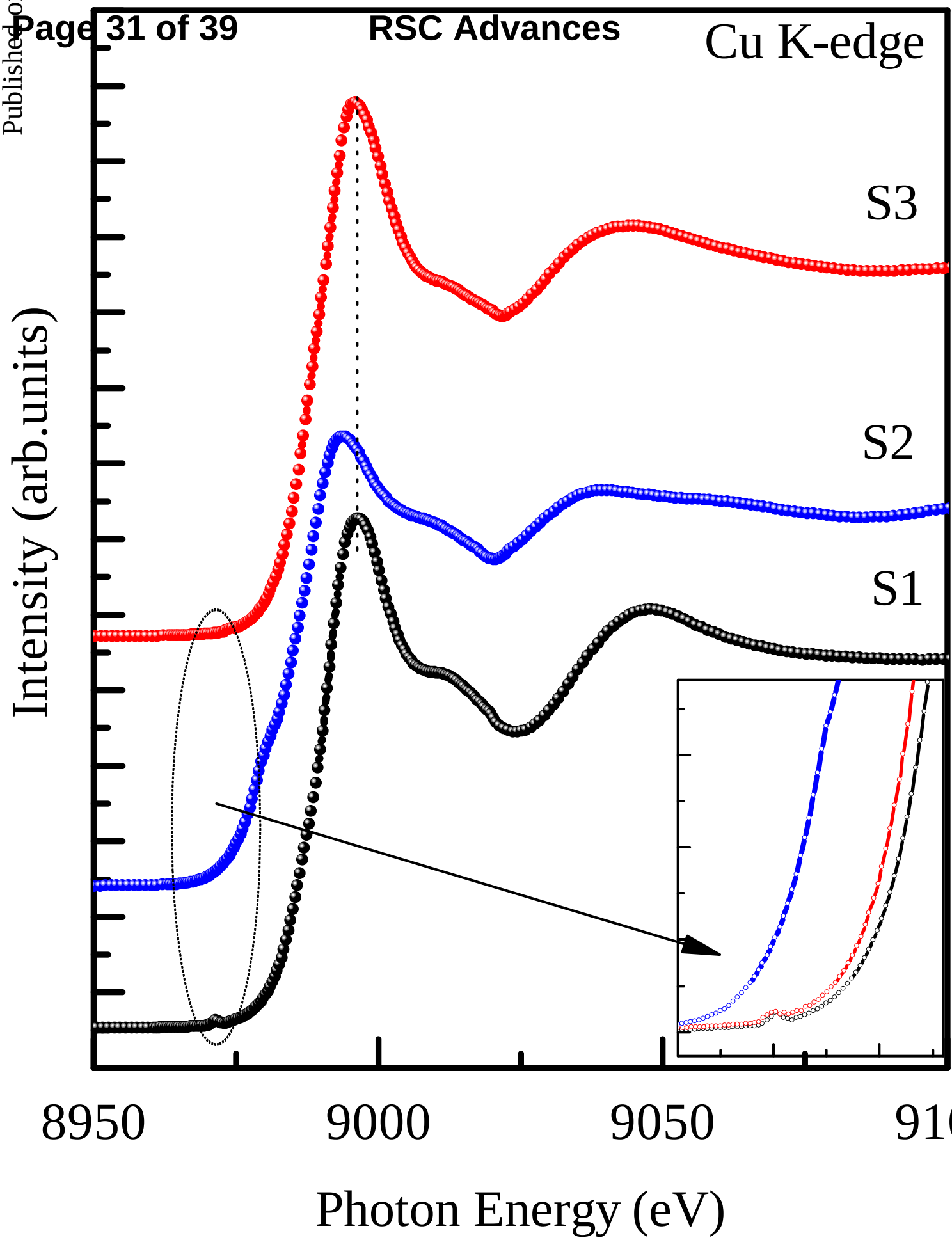

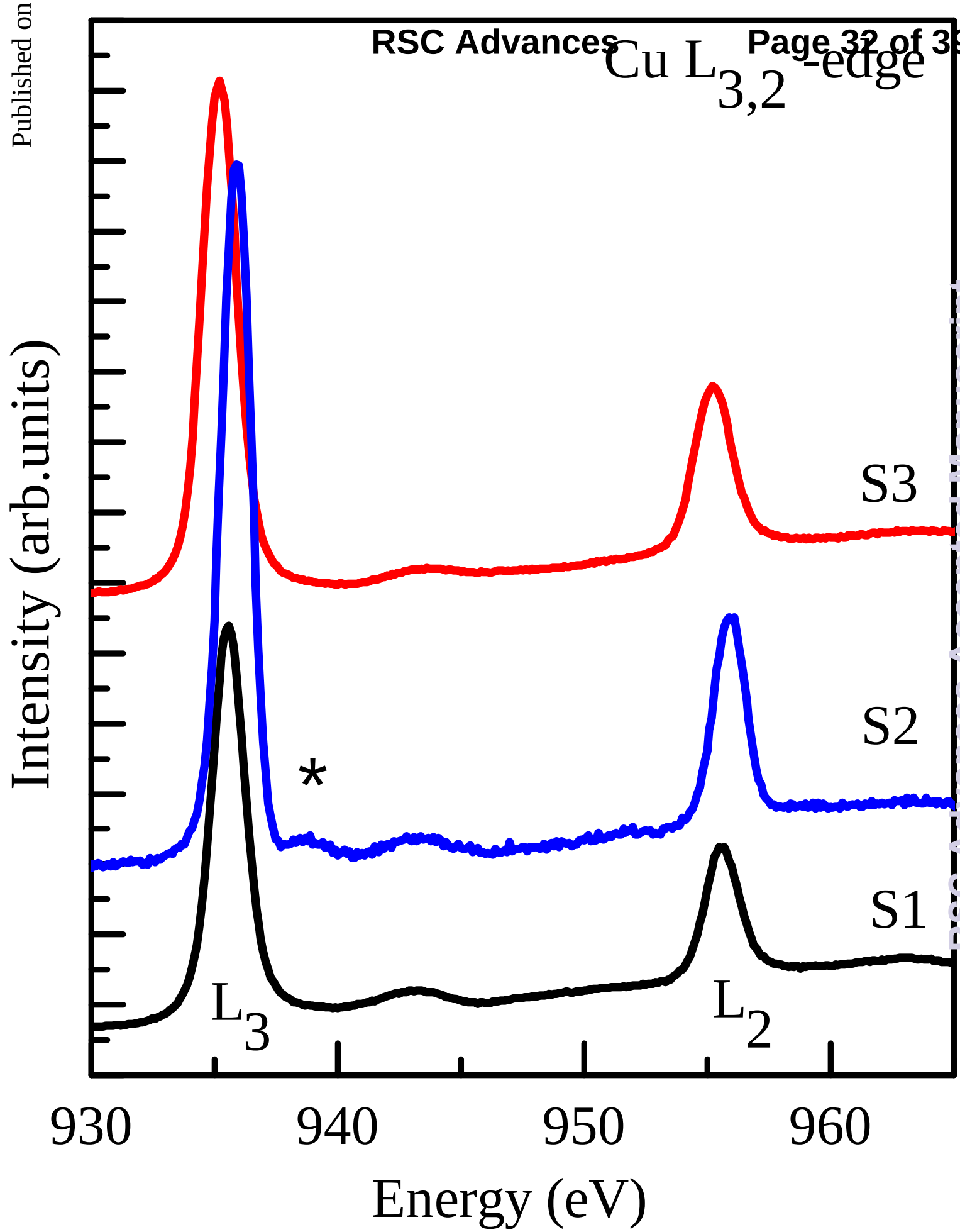

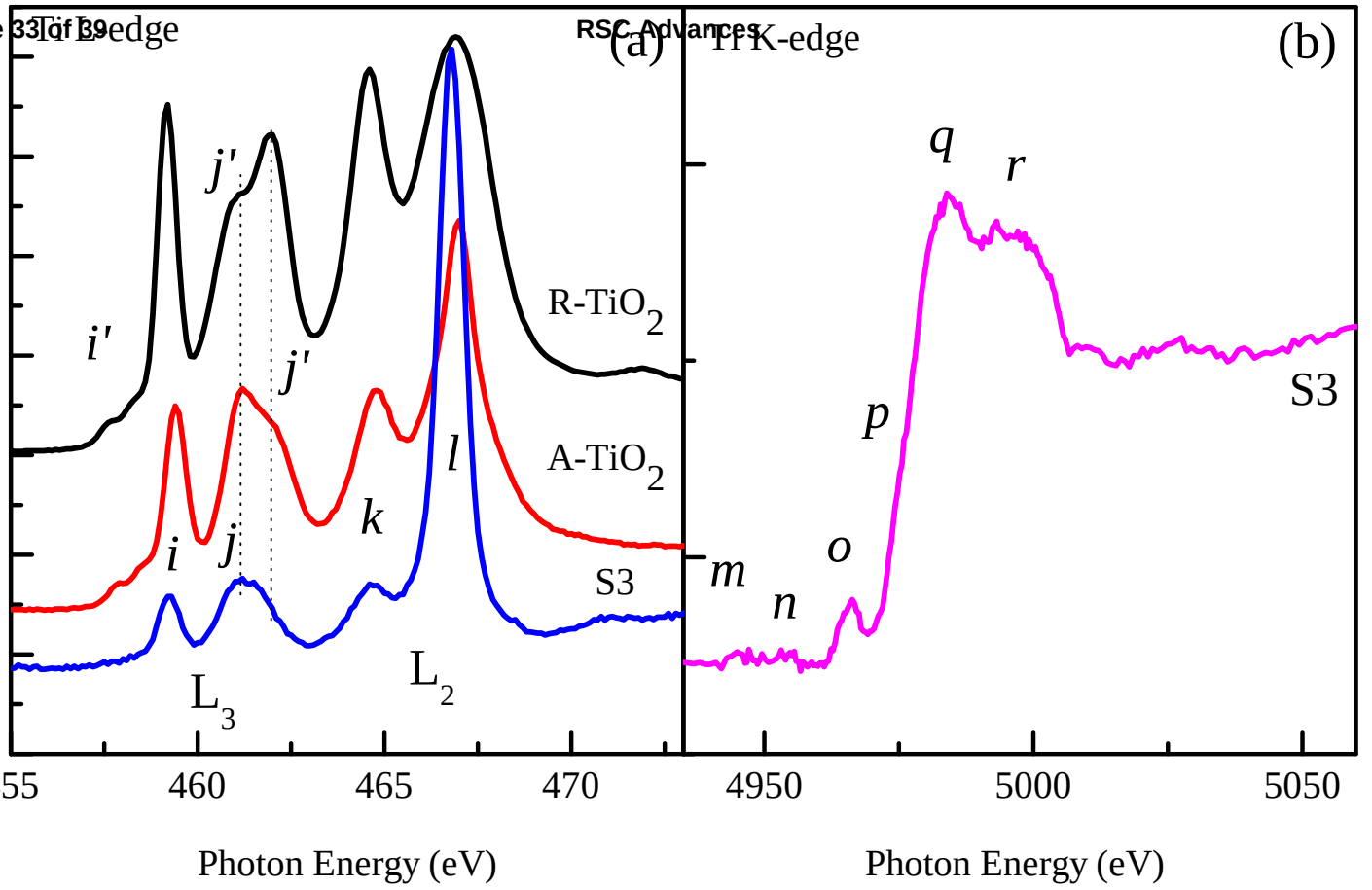

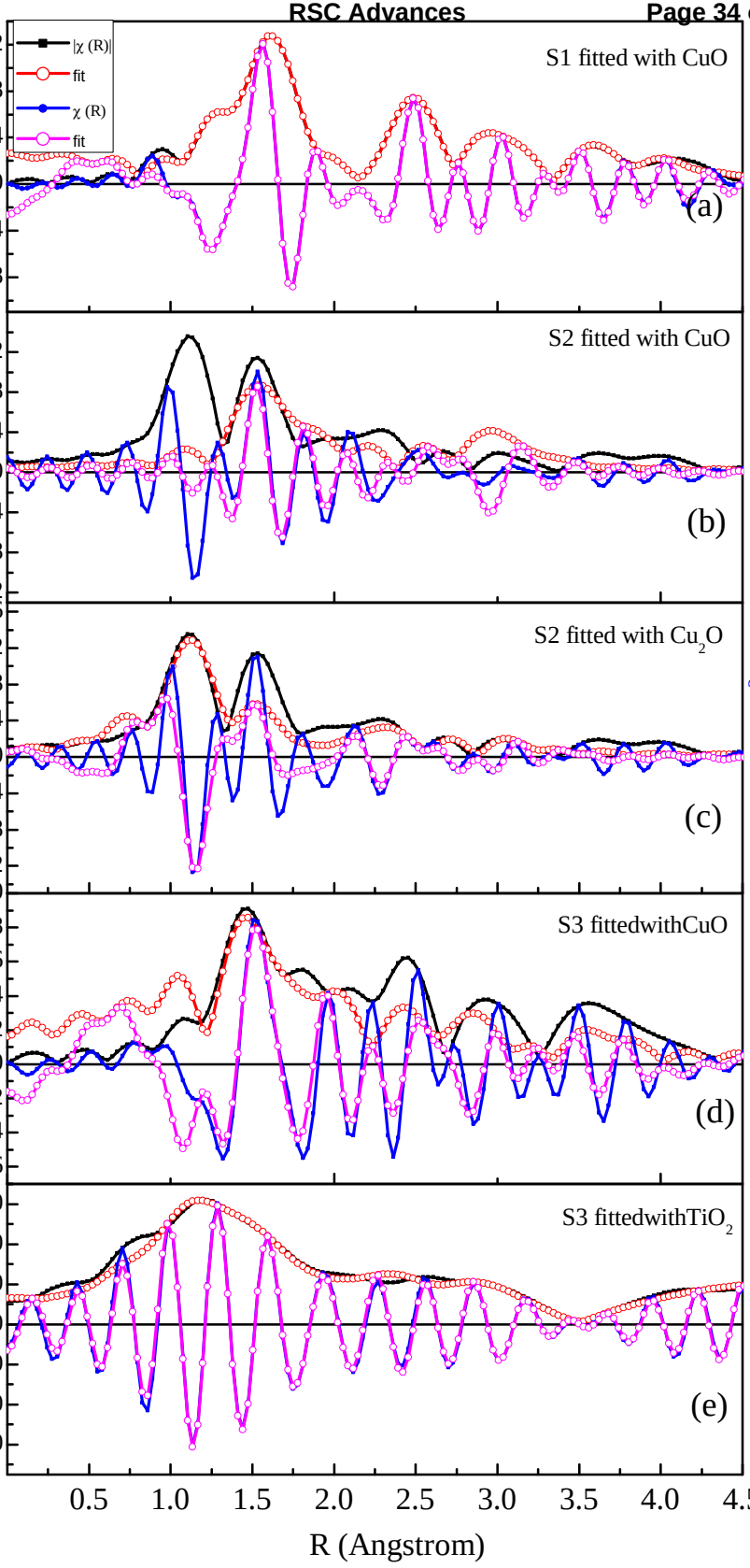

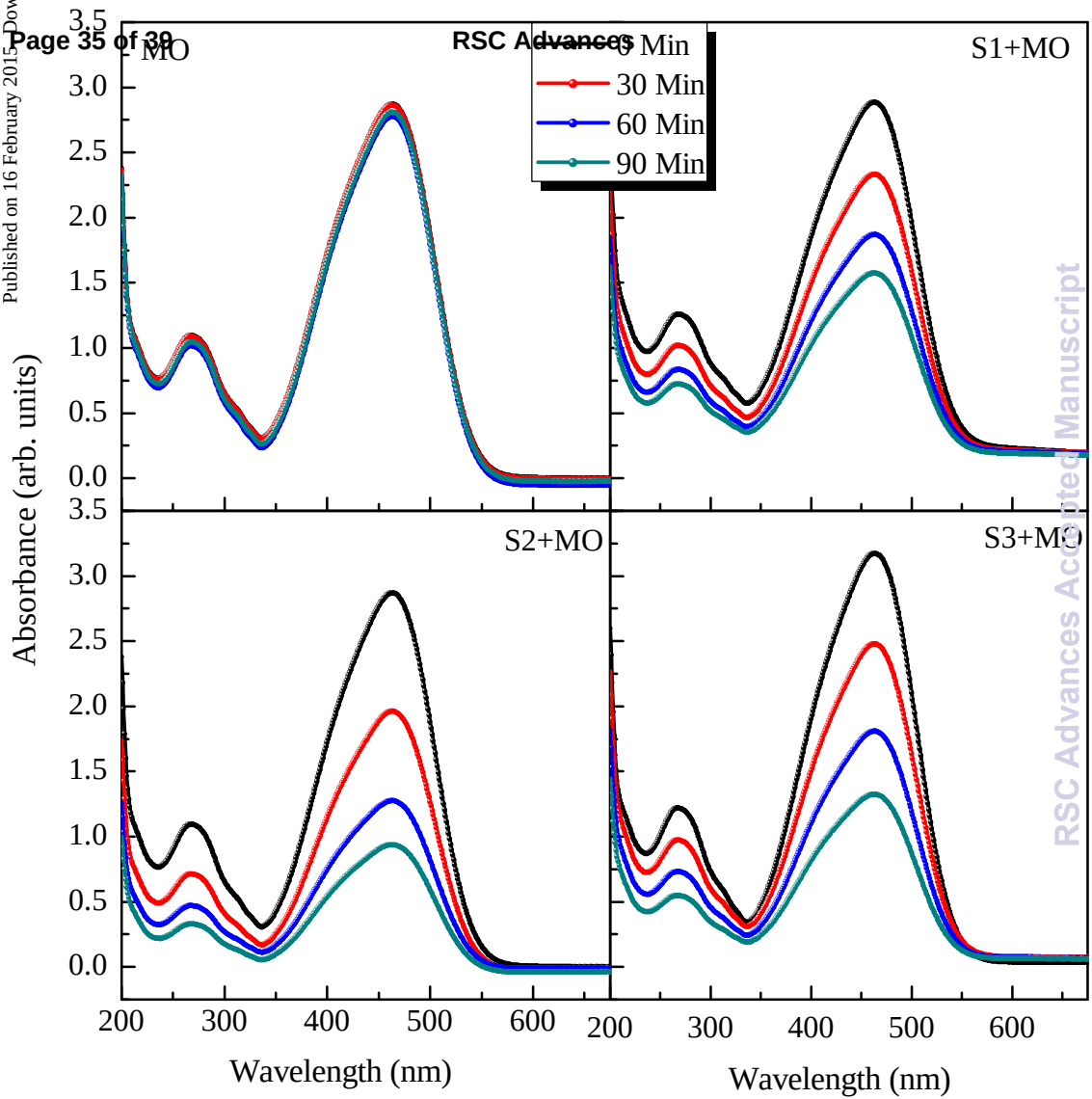

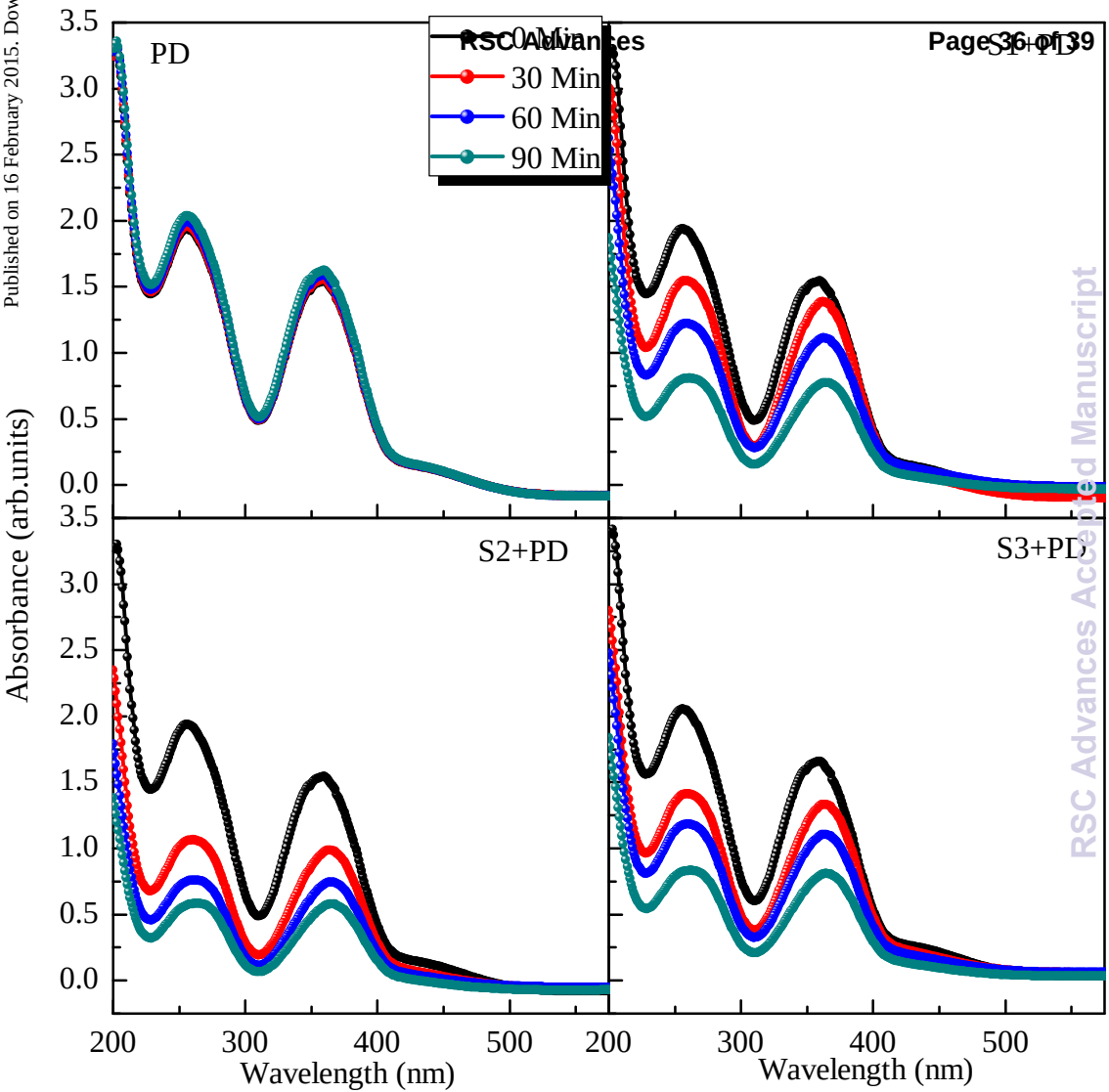

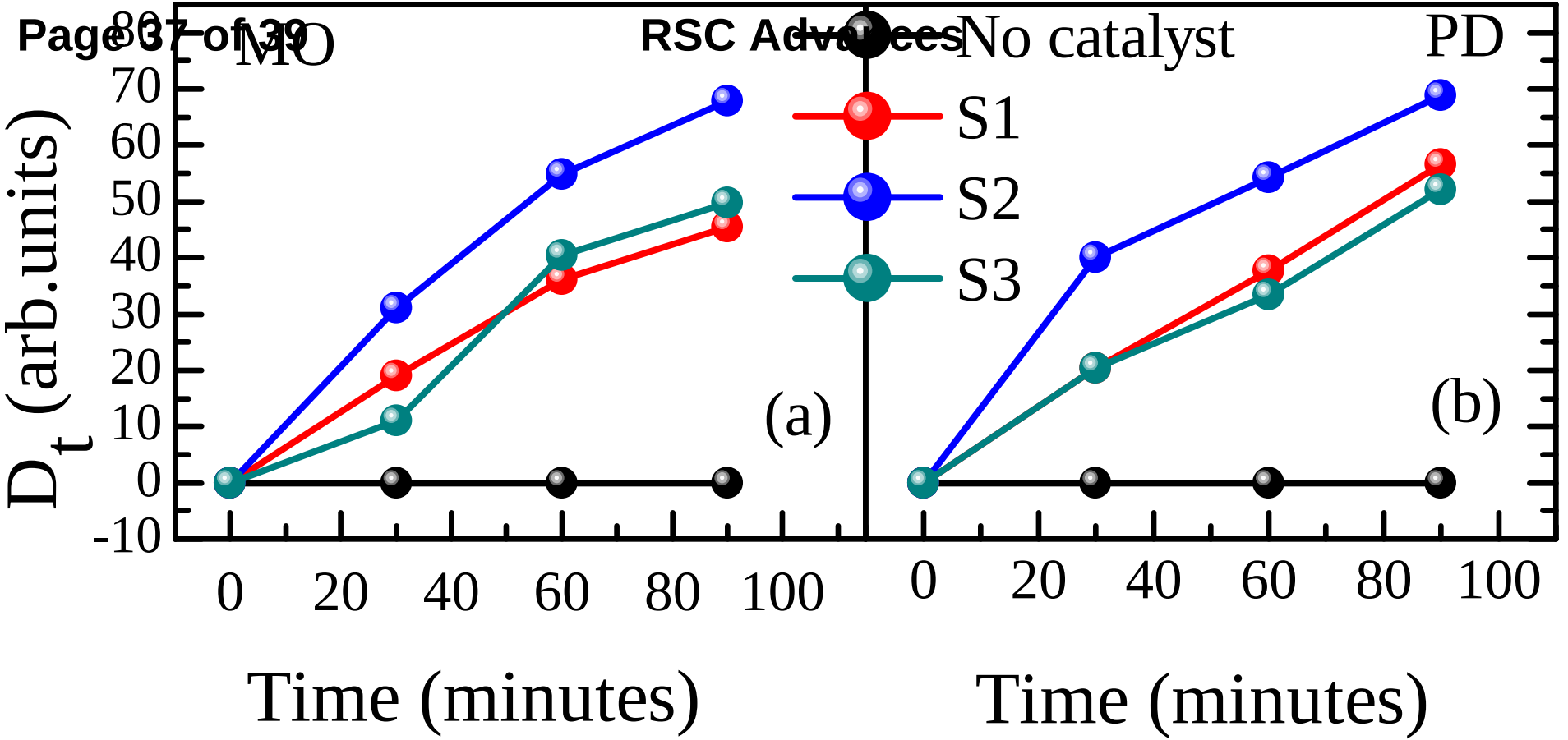

View Article Online
DOI: 10.1039/C4RA16217J

Preparation method	Used chemicals/materials	Sample name	Particle size (nm)		Product detail
			XRD	TEM	
co-precipitation (Scheme 1)	$Cu(CH3COO)_3.5H_2O$ + DI water + NH_4OH	S1	8.5	4.8-8.1	CuO
co-precipitation (Scheme 2)	$Cu(CH3COO)_3.5H_2O$ + DI water + PVA + NH_4OH	S2	6.2 (Cu_2O) 3.4 (CuO)	4-6.8	Cu_2O +CuO
co-precipitation (Scheme 3)	$Cu(CH3COO)_3.5H_2O$ + $TiCl_4.5H_2O$ + DI water + NH_4OH	S3	8.2 (CuO) 5.6 (TiO_2)	5.5-8	CuO+TiO_2

View Article Online
DOI: 10.1039/C4RA16217J

Sample Name	$Bond_{(compound)}$	R (Å)	CN	σ^2 (Å ^{2})
S1	$Cu - O_{(CuO)}$	1.91 ±0.015	3.81± 0.2	0.002
	$Cu - Cu_{(CuO)}$	2.89± 0.02	3.92±0.5	0.015
S2	$Cu - O_{(CuO)}$	1.90±0.015	3.22±0.5	0.125
	$Cu - Cu_{(CuO)}$	2.85±0.02	3.31±0.5	0.183
	$Cu - O_{(Cu_2O)}$	1.84±0.015	1.72±0.2	0.148
	$Cu - Cu_{(Cu_2O)}$	2.74±0.02	4.21±0.5	0.191
S3	$Cu - O_{(CuO)}$	1.92±0.02	3.80±0.5	0.154
	$Cu - Cu_{(CuO)}$	2.85±0.02	3.96±0.5	0.178
	$Ti - O_{(TiO_2)}$	1.98±0.01	4.6±0.5	0.002
	$Ti - Ti_{(TiO_2)}$	3.13±0.02	3.2±0.5	0.041
CuO	$Cu - O_{(CuO)}$	1.95	Ref. [42]	
Cu_2O	$Cu - O_{(Cu_2O)}$	1.86	Ref. [42]	